

# VLTI/GRAVITY Interferometric Measurements of Innermost Dust Structure Sizes around AGNs

GRAVITY Collaboration \*: A. Amorim<sup>1,2</sup>, G. Bourdarot<sup>3</sup>, W. Brandner<sup>4</sup>, Y. Cao<sup>3\*\*</sup>, Y. Clénet<sup>5</sup>, R. Davies<sup>3</sup>, P. T. de Zeeuw<sup>6</sup>, J. Dexter<sup>3,7</sup>, A. Drescher<sup>3</sup>, A. Eckart<sup>8,9</sup>, F. Eisenhauer<sup>3</sup>, M. Fabricius<sup>3</sup>, H. Feuchtgruber<sup>3</sup>, N. M. Förster Schreiber<sup>3</sup>, P. J. V. Garcia<sup>2,10,11</sup>, R. Genzel<sup>3,12</sup>, S. Gillessen<sup>3</sup>, D. Gratadour<sup>5,13</sup>, S. Hönig<sup>14</sup>, M. Kishimoto<sup>15</sup>, S. Lacour<sup>5,16</sup>, D. Lutz<sup>3</sup>, F. Millour<sup>17</sup>, H. Netzer<sup>18</sup>, T. Ott<sup>3</sup>, K. Perraut<sup>19</sup>, G. Perrin<sup>5</sup>, B. M. Peterson<sup>20</sup>, P. O. Petrucci<sup>19</sup>, O. Pfuhl<sup>16</sup>, M. A. Prieto<sup>21</sup>, S. Rabien<sup>3</sup>, D. Rouan<sup>5</sup>, D. J. D. Santos<sup>3</sup>, J. Shangguan<sup>3\*\*</sup>, T. Shimizu<sup>3</sup>, A. Sternberg<sup>18,22</sup>, C. Straubmeier<sup>8</sup>, E. Sturm<sup>3</sup>, L. J. Tacconi<sup>3</sup>, K. R. W. Tristram<sup>10</sup>, F. Widmann<sup>3</sup>, and J. Woillez<sup>16</sup>

(Affiliations can be found after the references)

Received ; accepted

## ABSTRACT

We present new VLTI/GRAVITY near-infrared interferometric measurements of the angular size of the innermost hot dust continuum for 14 type 1 AGNs. The angular sizes are resolved on scales of  $\sim 0.7$  mas and the inferred ring radii range from 0.028 to 1.33 pc, comparable to those reported previously and a factor 10-20 smaller than the mid-infrared sizes in the literature. Combining our new data with previously published values, we compile a sample of 25 AGN with bolometric luminosity ranging from  $10^{42}$  to  $10^{47}$  erg s<sup>-1</sup>, with which we study the radius-luminosity ( $R-L$ ) relation for the hot dust structure. Our interferometric measurements of radius are offset by a factor 2 from the equivalent relation derived through reverberation mapping. Using a simple model to explore the dust structure's geometry, we conclude that this offset can be explained if the  $2\ \mu\text{m}$  emitting surface has a concave shape. Our data show that the slope of the relation is in line with the canonical  $R \propto L^{0.5}$  when using an appropriately non-linear correction for bolometric luminosity. In contrast, using optical luminosity or applying a constant bolometric correction to it results in a significant deviation in the slope, suggesting a potential luminosity dependence on the spectral energy distribution. Over four orders of magnitude in luminosity, the intrinsic scatter around the  $R-L$  relation is 0.2 dex, suggesting a tight correlation between innermost hot dust structure size and the AGN luminosity.

**Key words.** galaxies: active – galaxies: nuclei – techniques:interferometric – galaxies: Seyfert

## 1. Introduction

The central engine of an active galactic nucleus (AGN) is powered by accretion onto a supermassive black hole (SMBH) with a mass that can be in the range from  $\sim 10^5 M_{\odot}$  in dwarf galaxies (Baldassare et al. 2015; Reines 2022; Mezcua & Sánchez 2024) to  $\sim 10^{10} M_{\odot}$  in the most massive galaxies (McConnell et al. 2011; Mehrgan et al. 2019). The UV photons from the accretion disk (Shakura & Sunyaev 1973) ionize the gas in its close proximity, forming the so-called broad line region (BLR). Dust sublimates on these scales (Barvainis 1987), but is an important component further out because of the key observational impact it has. It is found in disk, outflow, and filament structures in the innermost region surrounding the AGN which is responsible for significant nuclear obscuration (Antonucci & Miller 1985; Urry & Padovani 1995; Hönig 2019; Prieto et al. 2021). Much of the progress in our understanding of these inner structures of AGN has come about through substantial improvements in observational techniques (Netzer 2015). Notably, mid-infrared (MIR) and near-infrared (NIR) interferometry – here referred to as op-

tical/infrared interferometry (OI) – enables one to spatially resolve sub-parsec scales even in distant objects and is opening new opportunities for studies of AGN.

Long-baseline infrared interferometry has made it possible to delve into the detailed structure of dust by resolving its thermal emission at different wavelengths. At MIR wavelengths, interferometric observations of AGNs resolved warm dust structures emitting at a typical temperature of 400 K on scales of 3–30 mas (Kishimoto et al. 2011b; Burtscher et al. 2013). Contrary to the classical torus model, detailed modelling of the data has revealed a significant fraction of the total flux coming, in many sources, from the polar region containing graphite grain dust on parsec or larger scales (Hönig et al. 2013; López-Gonzaga et al. 2016; Leftley et al. 2018).

An alternate approach for investigating the dust structure is to monitor the time delay between the optical and NIR continuum emission. Using the time delay as an indicator of size, this reverberation mapping (RM) technique has measured the sizes of hot dust structures for  $\sim 30$  AGNs (e.g. Clavel et al. 1989; Suganuma et al. 2006; Koshida et al. 2014; Minezaki et al. 2019). At MIR wavelengths, the multi-epoch measurements of the WISE satellite (Wright et al. 2010) are also an effective way to measure time lags (Lyu et al. 2019; Yang et al. 2020; Mandal et al. 2024). These efforts have not only confirmed the general picture that the hot dust is outside the BLR (Clavel et al. 1989; GRAVITY Collaboration et al. 2023), but also that the time lag is smaller than predicted for the sublimation radius of standard ISM dust

\* GRAVITY is developed in a collaboration by the Max Planck Institute for Extraterrestrial Physics, LESIA of Observatoire de Paris/Université PSL/CNRS/Sorbonne Université/Université de Paris and IPAG of Université Grenoble Alpes/CNRS, the Max Planck Institute for Astronomy, the University of Cologne, the CENTRA – Centro de Astrofísica e Gravitação, and the European Southern Observatory.

\*\* Corresponding authors: Y. Cao (ycao@mpe.mpg.de) and J. Shangguan (shangguan@mpe.mpg.de)

composition and grain sizes. This offset implies the presence of large graphite dust grains and/or anisotropic illumination in the innermost region of the dusty structure (Kishimoto et al. 2007). In addition, the relation between the hot dust radius and AGN luminosity is found to be roughly  $R \propto L^{0.5}$  (Suganuma et al. 2006; Kishimoto et al. 2007), as expected for the simplest theoretical scenarios. Recent work indicates that the  $R$ – $L$  relation may be slightly shallower than the power of 0.5, although the physical reason for such a deviation is under debate (Minezaki et al. 2019; Sobrino Figaredo et al. 2020).

The sub-parsec NIR emission of typical type 1 AGNs has been successfully resolved with the Keck Interferometer (Swain et al. 2003; Kishimoto et al. 2009; Pott et al. 2010) and the Very Large Telescope Interferometer (VLTI; Weigelt et al. 2012). The sub-milliarcsec scales can be resolved by measuring the decrease of the visibility toward larger  $uv$  distance – which can be achieved with the baselines of 85 m for the Keck telescopes and 47–130 m for the Unit Telescopes (UTs) of the VLTI. More recently, Kishimoto et al. (2022) reported a new measurement of NGC 4151 at even longer baselines of  $\sim 250$  m using the CHARA array. The second-generation VLTI instrument GRAVITY (GRAVITY Collaboration et al. 2017), simultaneously combining the light from the four 8-m UTs over their size baselines, has vastly improved sensitivity and  $uv$  coverage. It has been able to spatially resolve the BLR of AGNs for the first time not only at low redshift (GRAVITY Collaboration et al. 2018, 2020b, 2021b,a, 2024) but also, with the recent upgrades toward GRAVITY+ (GRAVITY+ Collaboration et al. 2022), at  $z \sim 2$  (Abuter et al. 2024). In terms of hot dust emission, the first resolved image of the type 2 Seyfert NGC 1068 showed that it originates in a disk (GRAVITY Collaboration et al. 2020b), and combining this with mid-infrared interferometric data reveals it to be part of a disk plus outflow system (Gómez Rosas et al. 2022; Leftley et al. 2023).

NIR dust structure size measurements for about 10 AGNs, comparable to the total number observed previously, have been recently reported (GRAVITY Collaboration et al. 2020a,b; Leftley et al. 2021). Combined analyses of the available data have confirmed that the interferometric dust size ( $R_{\text{OI}}$ ) also follows a relation close to  $R \propto L^{0.5}$ , but that it is a factor 2 larger than the size inferred from the RM time lag ( $\tau_{\text{RM}}$ )<sup>1</sup> (Kishimoto et al. 2011a; Koshida et al. 2014; GRAVITY Collaboration et al. 2020a, 2023). The difference is not unexpected because the OI size reflects the projected light distribution, while the RM size includes additionally the response of the hot dust emission to the central heating source (Sobrino Figaredo et al. 2020). Moreover, RM is biased toward more compact structures as they respond more coherently than extended structures.

Here we take this work a step further by reporting new GRAVITY measurements of hot dust continuum sizes of 14 low- $z$  AGNs, significantly enlarging the interferometric AGN sample. We observed most of the targets with short exposures and reduced the data in a way that optimizes the continuum visibility (Section 2). We also carefully quantify the error budget on the measured size to take into account variations within a single night and between multiple nights (Section 3). The  $R$ – $L$  relation based on the full sample of OI measurements is discussed in Section 4. Employing a Monte Carlo model adaptable for exploring variations in observed OI and RM sizes with different dust structure geometries, we find a bowl-shape emitting hot dust surface can quantitatively explain the observed difference between

OI and RM sizes. The geometric covering factor and NIR colors of our favored model are also consistent with the observations (Section 5). Our main results are summarized in Section 6. We adopted the Planck Collaboration et al. (2016) cosmology:  $\Omega_m = 0.308$ ,  $\Omega_\Lambda = 0.692$ , and  $H_0 = 67.8 \text{ km s}^{-1} \text{ Mpc}^{-1}$ .

## 2. Observations and Data Reduction

### 2.1. Observations

The observation reported in this work come from two projects<sup>2</sup>: (1) The GRAVITY AGN Large Programme (PI: Sturm) has the primary goal of spatially resolving the broad-line region of bright ( $K < 11$ ) Seyfert 1 galaxies; (2) Our project focusing on the AGN hot dust continuum (PI: Davies). Due to the different primary science goals, the target observations adopted different setups. The observations of Akn 120, IC 4329A, Mrk 1239, Mrk 509, and PDS 456 were mainly to resolve the BLR with the spectro-astrometry technique. Therefore, we observed these targets with the single-field on-axis mode with light of the targets split in half into the science and fringe tracker (FT) channels, respectively. These targets were observed in multiple nights. The fringe tracker takes quick exposures (300 Hz) with only 6 channels over the  $K$  band to measure the coherence flux of the AGN within the coherence time of the atmosphere and is used for phase referencing the coherent integration of the science channel, where we adopted the MEDIUM ( $R = 500$ ) spectral resolution to measure the broad emission line. For the rest of the sources in this work, we only need FT data to resolve the hot dust continuum; therefore, our continuum-focused observations adopted the single-field off-axis mode with all of the target light used by the FT. Since the fringe tracker is limited by the brightness of the target, the single-field off-axis mode enables the observation of fainter targets than the single-field on-axis mode. We can usually measure the continuum size of a target with the single-field off-axis mode in one epoch with a  $\sim 1$  hour observation. The observation information of our targets are summarized in Table 1.

### 2.2. Data Reduction

We resolve the spatial extension of the hot dust continuum by measuring the drop of the visibility amplitude toward longer baselines. We first reduce the raw data of the AGN and the calibrator using the Python tool, `run_gravi_reduce`, of the GRAVITY pipeline (Lapeyrere et al. 2014) with all the default options except `--gravity_vis.p2vmreduced-file=TRUE`. The latter option is used to generate the intermediate data products (i.e. the P2VMRED files) that consist of the uncalibrated visibility data of each short FT exposure and other auxiliary data, such as the group delay (GDELAY) and geometric flux (F1F2), that can be used to flag the low quality data.

Previous works (GRAVITY Collaboration et al. 2020a; Leftley et al. 2021) found coherence loss of the visibility correlated with the Strehl ratio during the observation. This means that the measured visibility amplitude depends on the weather conditions and the performance of the adaptive optics. GRAVITY Collaboration et al. (2020a) found that it is effective to select exposures with group delay  $< 3 \mu\text{m}$  to alleviate the Strehl ratio dependence. Leftley et al. (2021) found, however, it is more effective to select exposures with the highest 3% geometric flux to alleviate the

<sup>1</sup> Hereafter, we use the term time lag exchangeably with  $R_{\text{RM}} \equiv c\tau_{\text{RM}}$  for simplicity.

<sup>2</sup> Observations were made using the ESO Telescopes at the La Silla Paranal Observatory, program IDs 1103.B-0626 and 0109.B-0270.

**Table 1.** Observation Log.

Name	Date	Observation Mode	Seeing (")	Coherence time (ms)	Strehl	$K$ (mag)	$V$ (mag)
(1)	(2)	(3)	(4)	(5)	(6)	(7)	(8)
Akn 120	2019-11-07	ON	0.37–0.76	5.4–10.2	0.04–0.09	10.8	13.9
IC 4329A	2021-02-01	ON	0.36–0.99	4.1–7.2	0.06–0.48	10.8	13.7
	2021-03-01	ON	0.43–0.78	3.7–9.4	0.04–0.13	10.6	
	2021-03-02	ON	0.62–0.95	4.7–7.0	0.03–0.11	10.3	
	2021-03-31	ON	0.70–0.82	3.1–4.1	0.06–0.14	10.3	
Mrk 1239	2021-01-30	ON	0.38–0.73	3.2–9.4	0.03–0.19	9.9	14.4
	2021-02-01	ON	0.32–0.44	5.0–15.5	0.14–0.31	10.2	
	2021-03-01	ON	0.66–1.05	3.1–7.8	0.02–0.09	10.1	
	2021-03-02	ON	0.46–0.85	4.6–6.5	0.02–0.12	9.5	
	2021-03-31	ON	0.48–0.94	2.5–5.5	0.02–0.14	9.5	
Mrk 509	2021-07-25	ON	0.50–0.80	2.5–4.2	0.05–0.23	11.2	13.1
	2021-07-26	ON	0.58–0.80	1.9–3.4	0.03–0.15	11.0	
NGC 7603	2021-07-26	OFF	0.58–0.71	2.3–3.3	0.02–0.09	10.8	14.0
PDS 456	2021-07-27	ON	0.54–0.82	2.9–4.6	0.03–0.13	11.0	14.0
PGC 89171	2021-07-26	OFF	0.61–0.73	2.4–3.2	0.05–0.14	11.1	14.4
UGC 545	2021-07-25	OFF	0.64–0.75	1.7–2.5	0.03–0.06	10.7	14.0
NGC 3227	2022-05-19	OFF	0.60–0.76	7.0–10.1	0.03–0.08	11.0	11.8
HE 1029–1401	2022-05-19	OFF	0.44–0.55	6.1–11.0	0.18–0.50	12.2	13.9
NGC 4593	2022-05-19	OFF	0.36–0.44	9.0–10.7	0.10–0.22	11.6	13.2
NGC 7469	2023-06-01	OFF	0.48–0.76	4.9–6.1	0.04–0.07	11.1	12.3
	2023-06-03	OFF	0.31–0.44	5.5–11.9	0.05–0.09	11.2	
IRAS 13349+2438	2023-06-06	OFF	0.57–0.70	11.0–13.4	0.07–0.13	10.1	15.0
UGC 11763	2023-06-06	OFF	0.54–0.83	5.8–7.0	0.10–0.17	11.4	14.6

**Notes.** Col. (1) Target name; Col. (2) Observation date; Col. (3) Observation mode, “ON” for on-axis mode with light spitted in half into the science and fringe tracker and “OFF” for off-axis mode with all of the light used by the fringe tracker; Col. (4)–(6) Averaged seeing, coherence time, and Strehl ratio during the observation. Col. (7) Nuclear  $K$ -band magnitude of the target measured by GRAVITY fringe tracker. The typical uncertainty is 0.2 mag based on our multiple exposures during the same night. Col. (8) Total  $V$ -band magnitude from Simbad.

AO loss for the data of ESO 323-G77. We tested both methods and find the selection based on the group delay performs better in general for our data. Using the group delay selection method, the rejection rate is substantially lower, typically around 50%, peaking at a maximum of 85%. Therefore, we choose to adopt the selection method of GRAVITY Collaboration et al. (2020a). We flag out the non-selected exposures in the P2VMRED files and use the Python tool `run_gravi_reduce_from_p2vmred` to generate the averaged uncalibrated visibility data. We adopt the same data selection for both AGN and calibrator data, although it does not affect the calibrator data because most of the calibrator exposures have  $GDELAY < 3 \mu\text{m}$ . Finally, we use the Python tool `run_gravi_trend` to calibrate the AGN data with those of the calibrator, in order to remove the remaining instrumental effects of the visibility data.

### 3. Hot dust size measurements

Interferometric resolution is determined by the baseline length  $B$  between telescopes and the observed wavelength  $\lambda$  as  $\lambda/2B$  (Eisenhauer et al. 2023); in the case of the UTs of the VLTI, the resolution reaches  $\sim 2$  mas in  $K$ -band. However, one can measure the size of an object with about 10 times better resolution by measuring how the contrast (or visibility) of the interferometric fringes decreases with larger baseline length (GRAVITY Collaboration et al. 2020a). In doing this, the squared visibility (VIS2DATA, hereafter  $V^2$ ) is used instead of the visibility am-

plitude (VISAMP) in the reduced GRAVITY FT data, because the former shows less coherence loss (GRAVITY Collaboration et al. 2020a; Leftley et al. 2021).

We measure the size of the hot dust by fitting the  $V^2$  of the FT continuum data to a Gaussian model,

$$V^2 = V_0^2 \exp\left(\frac{-\pi^2 r_{uv}^2 \text{FWHM}^2}{2 \ln 2}\right), \quad (1)$$

where  $V_0$  is the zero baseline visibility,  $r_{uv}$  is the baseline length in units of  $\text{mas}^{-1}$ , and FWHM in mas is the full width at the half maximum of the source emission. Following GRAVITY Collaboration et al. (2020a), we also allow  $V_0$  to be free in the fitting to account for the remaining coherence loss of the calibrated data and/or extended flux that is resolved out by the interferometer. We fit the visibility data from each individual exposure (with  $\sim 5$  minutes exposure time for the on-axis mode, and 2 minutes for the off-axis mode), and find the best-fitting zero baseline  $V_0$  and FWHM using the `scipy` function `curve_fit`. Figure 1 shows two such examples. The clear drops of  $V^2$  with increasing baseline lengths indicate that the hot dust continuum is resolved. We only incorporate the three central channels (2.07, 2.17, and  $2.27 \mu\text{m}$ ) of the FT data in the fitting because the remaining three channels are more susceptible to the detector background due to the metrology laser at the shorter wavelength and the thermal background at the longer wavelength.

We present the measured FWHM of each target in Table 2. We specifically include only those exposures for which the fitted

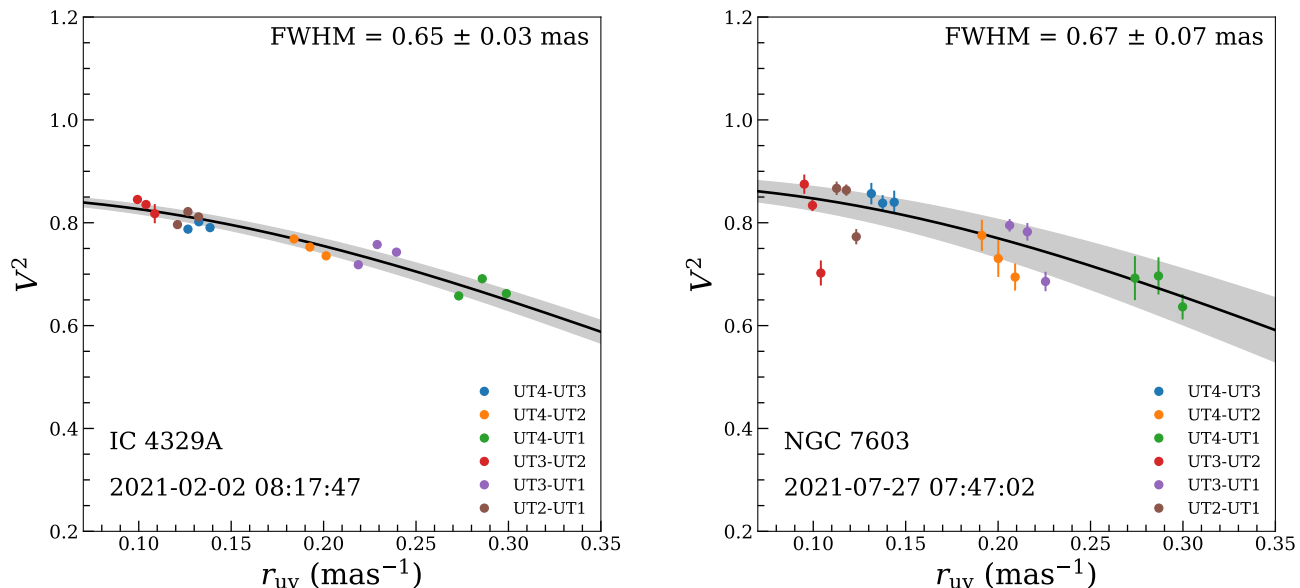


**Fig. 1.** FWHM visibility fitting for two single exposures. Colored dots with error bars show the visibilities measured at different baselines. Best fitting results from Equation 1 are shown in black solid lines, with the gray shaded region show the  $1\text{-}\sigma$  fitting uncertainties. The dates and the UT time are shown in the left bottom corners of each panel. The left panel illustrates a typical exposure, while the right panel shows an example of poor quality data.

error is less than one-third of the FWHM value. Subsequently, we calculate the median of these selected exposures to obtain the measured FWHM for each target. To estimate the FWHM uncertainty, GRAVITY Collaboration et al. (2020a) use the RMS of the FWHM from individual exposures and divide it by the square root of the number of nights. In this way, they account for the night-to-night systematic uncertainty, which likely comes from the variation of the AO performance. This method, however, cannot be applied to most of our targets because they were only observed once. Using the AGNs observed in multiple epochs to investigate the night-to-night FWHM variation, we find that it is about 10% of the averaged FWHM of each night. Therefore, we estimate the FWHM uncertainty by summing in quadrature two components: (1) the statistical uncertainty which is the RMS of FWHM values divided by the square root of the number of exposures; (2) the systematic uncertainty which is 10% of the median FWHM. Our method provides consistent FWHM uncertainties with that adopted by GRAVITY Collaboration et al. (2020a) for the targets observed with multiple nights.

Next, we convert the fitted Gaussian FWHM to a physical continuum radius. Following GRAVITY Collaboration et al. (2020a), we first convert the Gaussian FWHM to a ring radius by dividing by a factor of  $2\sqrt{\ln 2} \approx 1.67$ . We then correct for a putative contamination due to the unresolved central source (the accretion disk and/or jet) with a flux fraction of  $f$ , by scaling up the ring radius by a factor of  $1/\sqrt{1-f}$ . The flux fraction  $f$  differs for each object, and we use a typical constant value  $f = 20\%$  (Kishimoto et al. 2009) in our conversions into physical radii. Variation in  $f$  between different individual sources would introduce a small uncertainty ( $< 10\%$ ) to the derived sizes. The results are reported in Table 2.

At the end of the table, we provide updated measurements for two sources previously published in GRAVITY Collaboration et al. (2020a). The updated FWHM values remain consistent with the previous measurements ( $0.59 \pm 0.08$  for PDS 456

and  $0.54 \pm 0.06$  for Mrk 509). The reduction in uncertainties is attributed to the acquisition of additional exposures in 2021. Specifically, the updated sizes are based on approximately 1.5 times the number of exposures used for the previous published measurements.

**Table 2.** Angular and physical size measurements.

Source	FWHM (mas)	r (pc)
Akn 120	$0.70 \pm 0.09$	$0.328 \pm 0.040$
HE 1029-1401	$0.64 \pm 0.07$	$0.739 \pm 0.081$
IC 4329A	$0.64 \pm 0.02$	$0.151 \pm 0.004$
IRAS 13349+2438	$0.76 \pm 0.08$	$1.075 \pm 0.108$
Mrk 1239	$0.55 \pm 0.04$	$0.159 \pm 0.012$
NGC 3227	$0.50 \pm 0.06$	$0.028 \pm 0.004$
NGC 4593	$0.37 \pm 0.04$	$0.045 \pm 0.005$
NGC 7469	$0.74 \pm 0.04$	$0.178 \pm 0.008$
NGC 7603	$0.67 \pm 0.09$	$0.279 \pm 0.039$
PGC 89171	$0.65 \pm 0.07$	$0.254 \pm 0.027$
UGC 11763	$0.75 \pm 0.08$	$0.652 \pm 0.066$
UGC 545	$0.70 \pm 0.07$	$0.594 \pm 0.061$
PDS 456	$0.60 \pm 0.03$	$1.330 \pm 0.073$
Mrk 509	$0.62 \pm 0.03$	$0.304 \pm 0.017$

**Notes.** Angular FWHM sizes measured in this work, and corresponding physical sizes converted using a ring model. PDS 456 and Mrk 509 were published in GRAVITY Collaboration et al. (2020a) and we update the measured sizes combining both the new and previous observations.



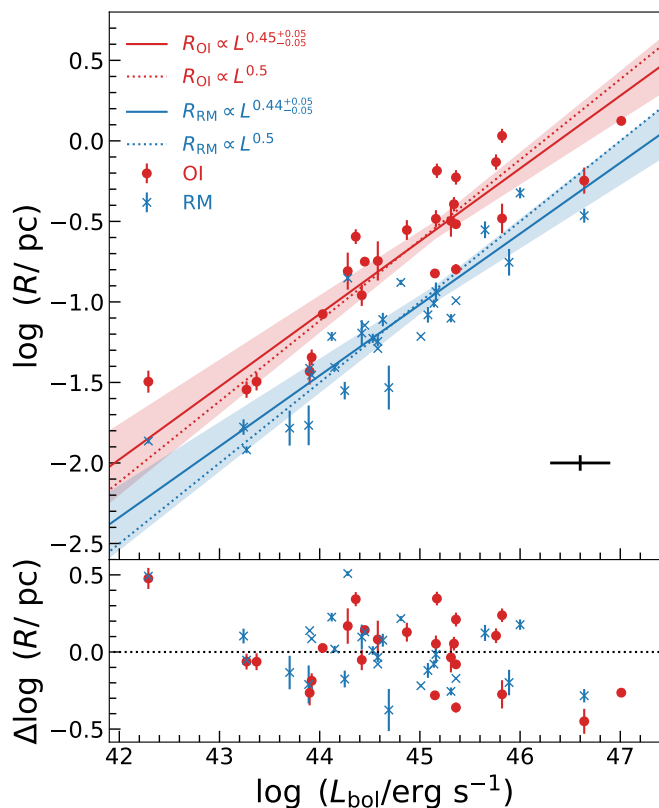


**Fig. 2.** Dust radius as a function of bolometric luminosity ( $R$ – $L_{\text{bol}}$  relation). OI measured sizes are shown in red and RM measured sizes are shown in blue. The typical 0.3 dex uncertainty in  $L_{\text{bol}}$  is indicated in the right corner. The solid lines show our best-fit results, with the shaded regions showing the  $1\text{-}\sigma$  uncertainties of the fittings, while the dotted lines represent the fitting results with the slopes  $m$  fixed to 0.5. Our best-fitted  $R$ – $L_{\text{bol}}$  relations are consistent with the slope of 0.5 within  $1\text{-}\sigma$ . The bottom panel shows the dust radius residuals from the fitted relation with fixed slopes of 0.5.

#### 4. Dust radius-luminosity relation

We measured the size of 12 new targets and updated 2 previous measurements with GRAVITY in this work. In Table 3 we compile from the literature all other dust size OI measurements in the K band obtained so far. The last four targets are observed by Keck, while all the others are observed by GRAVITY. IRAS 13349+2438 has been observed by both Keck and GRAVITY; the ring size we measure with GRAVITY is consistent with Keck measurement of  $0.92 \pm 0.06$  pc reported by Kishimoto et al. (2009). We choose to adopt the more recent result measured by GRAVITY for this study. The compiled data set allows us to study the dust radius-luminosity ( $R$ – $L$ ) relation. Together with the literature results, we compiled a sample of 25 type 1 AGNs with OI measured host dust structure sizes. For comparison, we also included 29 AGNs with an RM measured continuum size collected in Table 1 of our companion paper, GRAVITY Collaboration et al. (2023). In that paper, we collected the latest measurements of the hot dust continuum by OI and RM for  $z \lesssim 0.2$  AGNs, and our main focus was to investigate the relation between the BLR and the dust continuum size. Throughout this work, we adopted the continuum size directly converted from the time delay without applying any redshift correction (e.g. Minezaki et al. 2019), because the wavelength dependence of continuum emission size is expected to be less than 10% for our low- $z$  sample (GRAVITY Collaboration et al. 2023).

We collected the AGN luminosity from the literature following the method introduced in GRAVITY Collaboration et al. (2020a). Briefly, we collect the AGN 14–195 keV X-ray ( $L_{14\text{--}195\text{keV}}$ ), optical (5100 Å,  $\lambda L_{\lambda}(5100\text{\AA})$ ), and 12  $\mu\text{m}$  ( $\lambda L_{\lambda}(12\mu\text{m})$ ) monochromatic luminosities whenever available. The X-ray luminosity comes from the Swift/BAT observations (Baumgartner et al. 2013). We discarded the X-ray luminosities of 3C 273 and PDS 456 due to contamination from jet emission and significant variability, respectively. The optical luminosities are taken from GRAVITY Collaboration et al. (2023), and the  $\lambda L_{\lambda}(12\mu\text{m})$  comes from the high resolution MIR observations by Asmus et al. (2011).

Fundamentally the dust is heated by the central optical/UV continuum source, and thus the size is expected to depend on the total optical-to-UV luminosity (Barvainis 1987). However, measuring optical-to-UV luminosity is challenging due to various factors. We opt to use the bolometric luminosity that can be derived from various methods. As detailed in Appendix A, we calculated  $L_{\text{bol}}$  based on 14–195 keV measurements whenever possible, using non-linear corrections. In cases where such measurements are unavailable, we opt for values derived from the optical luminosity (see Table A.1 for details). We include the  $\lambda L_{\lambda}(12\mu\text{m})$  to provide additional comparison to quantify the uncertainty of the bolometric luminosities and the  $R$ – $L$  relations. The differences in  $L_{\text{bol}}$  estimates from different monochromatic luminosities agree to within 0.3 dex, which we adopt as the uncertainty.

We fit the  $R$ – $L$  relations of the bolometric luminosity and various monochromatic luminosities in the form of Equation 2 using the `linmix` package, which is a Python version of `LINMIX_ERR` from Kelly (2007),

$$\log R = c + m \log \left( \frac{L}{L_0} \right), \quad (2)$$

where  $c$  and  $m$  are the regression intercept and slope respectively,  $R$  is the measured dust continuum size in pc,  $L$  is the luminosity, and  $L_0$  is fixed at the same value for both the OI and RM relations to reduce the degeneracy of the regression coefficients. In `LINMIX_ERR`, the probability distribution of the independent variable is modeled as a mixture of  $K$  Gaussian functions, and we choose  $K = 2$  for all of our fittings throughout this work. We use the median values of the  $c$  and  $m$  coefficients obtained from the likelihood distributions generated by `LINMIX_ERR` as the best-fit regression coefficients. The uncertainties associated with these coefficients are determined from the 16% and 84% percentiles of their likelihood distributions. We also characterize the intrinsic scatter of the linear regression,  $\sigma_{\text{intrinsic}}$ , using the median value from its distribution. The best-fit parameters with uncertainties are listed in Table 4.

We first fit the dust size  $R$  as a function of bolometric luminosity. Figure 2 shows the relation of  $R$ – $L_{\text{bol}}$  to the continuum sizes measured by the OI and RM, respectively. The best-fitted slope for  $R_{\text{OI}}$  is about 0.45, slightly shallower than, but consistent within  $\sim 1\sigma$  of, the expected  $R \propto L^{0.5}$ . The best-fit slope for  $R_{\text{RM}}$  is entirely consistent with that of  $R_{\text{OI}}$ . The uncertainty of the slope can be further reduced by expanding the sample with high and low luminosities. The intrinsic scatter for the  $R_{\text{OI}}$  relation is 0.2 dex, similar to that of the  $R_{\text{RM}}$  relation. We do not find a significant correlation between the offsets from the fitted dust  $R$ – $L$  relation and the Eddington ratio with the OI measurements.

Our compilation of the literature measurements cannot guarantee that the continuum size and the AGN luminosities are measured close in time. Kishimoto et al. (2013) showed in NGC

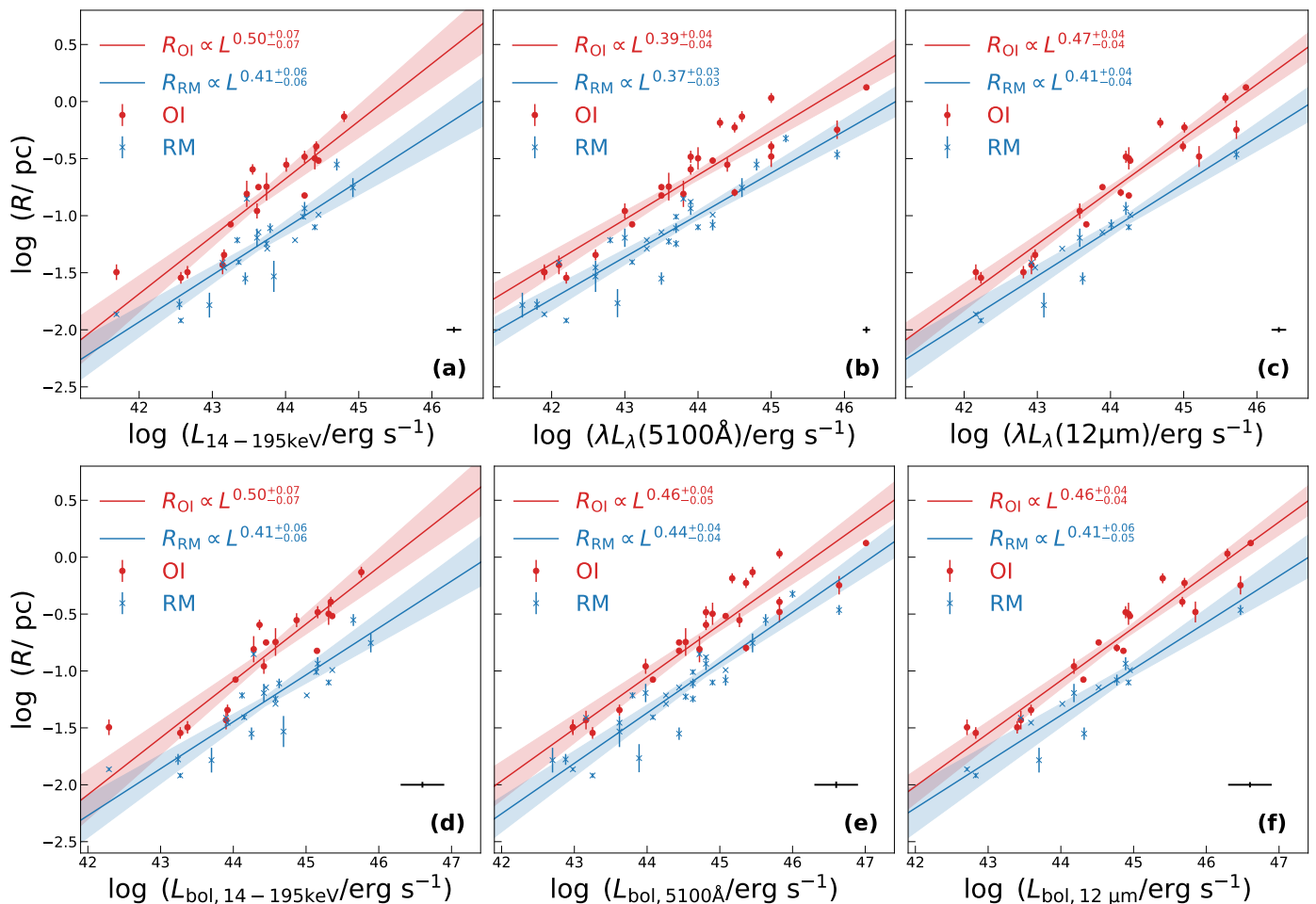


**Fig. 3.** The top panels show the relations between the dust size and the monochromatic luminosities at (a) 14–195 keV, (b) optical 5100 Å, and (c) 12 μm. The lower panels (d)–(f) show the  $R$ – $L$  relation of the bolometric luminosity converted from these three monochromatic luminosities respectively. The symbols are the same as Figure 2. The slopes of the relations using RM and OI measurements agree with each other in all kinds of luminosities we investigated. For OI measurements, all the  $R$ – $L$  relationships agree within one sigma with a slope of 0.5, except for the optical luminosity  $\lambda L_{\lambda}(5100\text{\AA})$ .

4151 that any change in luminosity will not immediately affect the measured dust sublimation radius, only if the change persists over several years. A potential explanation for this reduced response to AGN variability proposed by Hönl & Kishimoto (2011), is the “snowball” model, in which clouds only gradually sublimate at the inner edge of the torus. In this case the dust size may be relatively constant with time in a typical AGN, and the AGN variability itself may be the dominant source of intrinsic scatter (see more discussion in GRAVITY Collaboration et al. 2023).

We also fit the  $R$ – $L$  relations using different monochromatic luminosities ( $L_{14-195\text{keV}}$ ,  $\lambda L_{\lambda}(5100\text{\AA})$ , and  $\lambda L_{\lambda}(12\mu\text{m})$ ) and their corresponding bolometric luminosity following the equations in Appendix A. Using monochromatic luminosities separates SED effects which potentially influence dust structure size, while converting them to  $L_{\text{bol}}$  with appropriate bolometric corrections aligns  $R$ – $L$  relations across wavelengths, mitigating differences related to the observed luminosity’s wavelength. The results for all these  $R$ – $L$  relations are shown in Figure 3 and Table 4.

As in Figure 2, we find that the slopes of the OI-measured  $R$ – $L$  relations consistently agree with those of the RM-measured relations for each type of luminosity in Figure 3. For monochromatic luminosities shown in the top row of Figure 3, the slopes of the relations vary with wavelength, probably due to the

SED change as a function of luminosity. The slopes of the  $\lambda L_{\lambda}(5100\text{\AA})$   $R$ – $L$  relation in panel (b) shows the most significant deviation from the 0.5 power law, which is close to  $3\text{-}\sigma$ . This finding is consistent with previous studies from Minezaki et al. (2019) and Sobrino Figaredo et al. (2020). Various explanations have been discussed by these authors to interpret the observed shallower slope, such as anisotropic illumination by the accretion disk, non-trivial composition and geometry of the dust structure delayed dust sublimation responses and nonlinear correlations between optical and UV luminosities. For detailed discussions and references of these interpretations, we direct the readers to Minezaki et al. (2019) and Sobrino Figaredo et al. (2020).

On the other hand, we find that  $R$ – $L$  relations using bolometric luminosities derived from optical luminosities with nonlinear bolometric corrections show slopes consistent with the canonical  $R \propto L^{0.5}$  relation within  $1\text{-}\sigma$  (notably panel (e) in Figure 3). Indeed, for OI measurements, the slopes of the  $R$ – $L$  relations fitted using bolometric luminosities are all in line with canonical value of 0.5. Therefore we suggest that comparing the slope of the  $R$ – $L$  relation observed using monochromatic luminosities (or a simple linear bolometric correction) to the canonical value of 0.5 may be misleading. This is because the relation between monochromatic luminosities and dust heating is sensitive

**Table 3.** Literature physical size measurements.

Source	$R_{\text{OI}}$ (pc)	Ref
3C 120	$0.318 \pm 0.071$	1
3C 273	$0.567 \pm 0.106$	1
ESO 323-G77	$0.084 \pm 0.004$	2
IRAS 09149-6206	$0.405 \pm 0.041$	1
Mrk 335	$0.155 \pm 0.041$	1
NGC 1365	$0.032 \pm 0.004$	1
NGC 3783	$0.110 \pm 0.017$	1
Mrk 231	$0.330 \pm 0.070$	3
Mrk 6	$0.180 \pm 0.050$	4
NGC 4051	$0.032 \pm 0.005$	3
NGC 4151	$0.037 \pm 0.007$	4

**References:** (1) GRAVITY Collaboration et al. (2020a) (2) Leftley et al. (2021) (3) Kishimoto et al. (2009) (4) Kishimoto et al. (2011a)

to the SED shape. The adopted non-linear bolometric correction in our approach, which results in steeper slopes than the monochromatic  $R$ – $L$  relations, may reflect the systemic dependency of SED shape on luminosities (e.g. Vignali et al. 2003; Netzer 2019; Duras et al. 2020).

Recent RM studies using WISE  $W1$  ( $3.4 \mu\text{m}$ ) and  $W2$  ( $4.6 \mu\text{m}$ ) data support our conclusion. Several works (Chen et al. 2023; Mandal et al. 2024) reporting their  $R$ – $L$  relation slope shallower than 0.5, either used the  $\lambda L_{\lambda}(5100\text{\AA})$  or a  $V$ -band luminosity with a constant bolometric correction. In contrast, Lyu et al. (2019) applied a nonlinear bolometric correction, albeit different from our approach, and reported a slope similar to our result. Similar differences in slopes between  $\lambda L_{\lambda}(5100\text{\AA})$  and  $L_{\text{bol}}$  are also evident in the BLR  $R$ – $L$  relations (Abuter et al. 2024). For studying the  $R$ – $L$  relations, we recommend using the more accurate nonlinear correction (e.g., Netzer 2019; Duras et al. 2020) rather than a linear approximation for the bolometric luminosities.

In all the fits of  $R$ – $L$  relations we have examined, the intrinsic scatters are predominantly below 0.2 dex. Typically, the intrinsic scatters from monochromatic luminosities are slightly larger than those from bolometric luminosities. This may be due to the larger uncertainty assigned to the bolometric luminosities, while the larger scatter in the monochromatic luminosities likely reflects the specific characteristics of individual sources’ SEDs. Contamination of NIR continuum from compact jet emission in some sources (Fernández-Ontiveros et al. 2023) could also contribute to the scatter in the  $R$ – $L$  relations. Additionally, the intrinsic scatter is influenced by the range of luminosities and the number of data points used for the fitting. For instance, the higher intrinsic scatter from  $L_{14-195\text{keV}}$  is likely due to the small range of luminosity, because of the lack of high luminosity objects in this sample. Additionally, a smaller range of luminosity also introduces a larger uncertainty on the fitted slopes. Nevertheless, the relatively small intrinsic scatter from all the relations indicates that the  $R$ – $L$  relations are tightly constrained.

## 5. Constraining the hot dust structure

The  $R$ – $L$  relations from both OI and RM measurements have similar slopes. However, there is a general offset between the two relations. As shown in Table 4, the intercepts ( $m$ ) fitted from OI data are  $\sim 0.3$ – $0.4$  dex larger than those from the RM method.

This means the hot dust continuum size measured by OI is in general about 2–2.5 times larger than that measured by the RM time lag. It has been attributed to the difference between the flux-weighted radius and response-weighted radius of the innermost hot dust (Koshida et al. 2014). Moreover, Sobrino Figaredo et al. (2020) argue that the large  $R_{\text{OI}}/R_{\text{RM}}$  ratio can be explained by the “foreshortening effect” of a bowl-shape dust structure (Pozo Nuñez et al. 2014; Oknyansky et al. 2015; Ramolla et al. 2018). In this section, we adopt a simple model of hot dust emission to explore how the observed  $R_{\text{OI}}/R_{\text{RM}}$  can be used to constrain the model. Our goal is to obtain qualitative properties of the hot dust structure based on the samples of OI and RM observations, while more quantitative measurements of the hot dust structure of individual sources must be obtained by modeling of the OI and RM data in detail.

We incorporate a simple model as described in Guise et al. (2022). The hot dust emission comes from a 2-D surface which can be flaring above the midplane as shown in Figure 4. The model is flexible enough to generate the bowl-shape structure which was proposed previously (e.g. Kawaguchi & Mori 2010; Goad et al. 2012) and supported by RM observations (e.g. Pozo Nuñez et al. 2014; Oknyansky et al. 2015; Ramolla et al. 2018; Sobrino Figaredo et al. 2020). The model assumes that the dust distribution is optically thick in the vertical direction, so that the IR emission is dominated by the surface of the structure facing the observer. The details of the model are summarized in Appendix B. Briefly, the model consists of a large number of dust clouds, each in thermal equilibrium and radiating as blackbodies. The cloud radial distribution is controlled by a power-law index  $\alpha$ , while cloud heights above the midplane are controlled by another power-law index  $\beta$ . A higher  $\alpha$  means more emission from the outer region, while the curved surface will become steeper with a larger  $\beta$ . The model is observed at an inclination angle  $i$ . Only one side of the dust emission can be observed because the other side, which is behind the midplane, is fully obscured in NIR (See Appendix B for adopted dust temperature and spectral energy distribution (SED)). As illustrated by Figure 4 (assuming  $i = 0^\circ$  with the line of sight downward from the top for simplicity), the bowl-shape (one-sided) dust emission naturally leads to an RM time lag smaller than the projected size of the hot dust, the “foreshortening effect” (Sobrino Figaredo et al. 2020; and references therein). To account for the observational effect that we measure the size of the hot dust interferometrically, we simulate the  $V^2$  of the model assuming a typical size, distance, and baseline lengths of our targets. We measure the  $R_{\text{OI}}$  of the simulated  $V^2$  in the same way as our targets, by fitting a Gaussian model and converting the FWHM to a ring radius (see details in Section 3); we do not apply additional correction for the central point source, as the model does not incorporate its flux contribution. Meanwhile the time lag ( $R_{\text{RM}} \equiv c\tau_{\text{RM}}$ ) is calculated as the flux-weighted mean time lag of all the dust clouds. Both the sizes  $R_{\text{OI}}$  and  $R_{\text{RM}}$  are in units of the dust sublimation radius  $r_{\text{sub}}$ . Exploration of the parameter space shows that such a model can easily reproduce  $R_{\text{OI}}/R_{\text{RM}} \approx 2$  while other properties of the model match various independent observational constraints.

As shown in Figure 5, we calculate the  $R_{\text{OI}}/R_{\text{RM}}$  ratio of the model with  $-0.5 < \alpha < 2.0$  and  $0 < \beta < 2.0$  viewed with inclinations of  $0^\circ$ ,  $10^\circ$ ,  $20^\circ$ , and  $40^\circ$ . To guide the eye, we highlight a fiducial model with  $\alpha = 1.0$  and  $\beta = 1.0$ , which corresponds to a conical structure. The corresponding  $R_{\text{OI}}/R_{\text{RM}}$  decreases from around 2.5 to around 1.5 when the inclination increases from  $0^\circ$  to  $40^\circ$ . At fixed inclination, the ratio increases when  $\alpha$  and  $\beta$  increase because more emission comes further away from the midplane and the foreshortening effect is stronger. When  $\alpha \gtrsim 1$ , the

**Table 4.** Results of linear regression of R-L relations for OI and RM measurements

$L$	Definition	$\sigma_{\log L}$	$\log(L_0/\text{erg s}^{-1})$	$R$	$N$	$c$	$m$	$\sigma_{\text{intrinsic}}$
$L_{\text{bol}}$	Bolometric luminosity in this work	0.3	45.1	OI	25	$-0.55^{+0.05}_{-0.05}$	$0.45^{+0.05}_{-0.05}$	0.20
				RM	29	$-0.95^{+0.05}_{-0.05}$	$0.44^{+0.05}_{-0.05}$	0.15
$L_{14-195 \text{ keV}}$	14 – 195 keV luminosity	0.1	43.6	OI	18	$-0.87^{+0.05}_{-0.05}$	$0.50^{+0.07}_{-0.07}$	0.21
				RM	23	$-1.26^{+0.04}_{-0.04}$	$0.41^{+0.06}_{-0.06}$	0.19
$\lambda L_{\lambda}(5100 \text{ \AA})$	Monochromatic luminosity at 5100 Å	0.05	43.9	OI	25	$-0.68^{+0.04}_{-0.04}$	$0.39^{+0.04}_{-0.04}$	0.20
				RM	29	$-1.03^{+0.04}_{-0.04}$	$0.37^{+0.03}_{-0.03}$	0.17
$\lambda L_{\lambda}(12 \mu\text{m})$	Monochromatic luminosity at 12 μm	0.1	44.2	OI	20	$-0.68^{+0.04}_{-0.04}$	$0.47^{+0.04}_{-0.04}$	0.16
				RM	14	$-1.03^{+0.05}_{-0.05}$	$0.41^{+0.04}_{-0.04}$	0.14
$L_{\text{bol},14-195 \text{ keV}}$	Bolometric luminosity from $L_{14-195 \text{ keV}}$	0.3	44.4	OI	18	$-0.87^{+0.05}_{-0.05}$	$0.50^{+0.07}_{-0.07}$	0.16
				RM	23	$-1.27^{+0.04}_{-0.04}$	$0.41^{+0.06}_{-0.06}$	0.16
$L_{\text{bol},5100\text{\AA}}$	Bolometric luminosity from $L_{\lambda}(5100 \text{ \AA})$	0.3	44.8	OI	25	$-0.68^{+0.04}_{-0.04}$	$0.46^{+0.04}_{-0.05}$	0.16
				RM	29	$-1.01^{+0.04}_{-0.04}$	$0.44^{+0.04}_{-0.04}$	0.12
$L_{\text{bol},12\mu\text{m}}$	Bolometric luminosity from $L_{\lambda}(12 \mu\text{m})$	0.3	44.9	OI	20	$-0.68^{+0.04}_{-0.04}$	$0.46^{+0.04}_{-0.04}$	0.11
				RM	14	$-1.03^{+0.05}_{-0.06}$	$0.41^{+0.06}_{-0.05}$	0.12

**Notes.**  $R$  is the type of the dust size measurements.  $N$  is the number of the data pair of each fitting, depending on the data availability of each kind of luminosity measurement.  $L_0$ ,  $c$ , and  $m$  are defined in Equation 2, and  $\sigma_{\text{intrinsic}}$  is the intrinsic scatter about the relation.

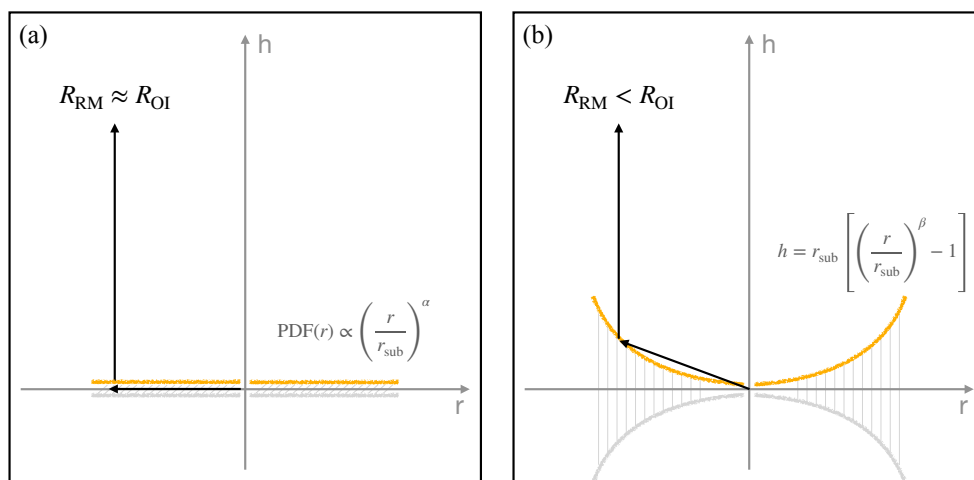


**Fig. 4.** The sketch of the hot dust structure model. The hot dust emission is in yellow. The cloud radial distribution follows a power law with the index  $\alpha$ , and the cloud height above the midplane is close to a power-law function controlled by  $\beta$ . Panel (a) shows the model with  $\beta \approx 0$ , while panel (b) shows a model with  $\beta > 0$ . We show the models in an edge-on view with the observer to the positive direction of  $h$  to illustrate the foreshortening effect. In this way, model (a) has  $R_{\text{RM}} \approx R_{\text{OI}}$ , while model (b) has  $R_{\text{RM}} < R_{\text{OI}}$ .

$R_{\text{OI}}/R_{\text{RM}}$  ratio mainly depends on  $\beta$  because the hot dust emission mainly comes from the outer edge of the model.

The model parameters can be further constrained by our other knowledge from observation and theory. Within our preferred parameter space,  $R_{\text{RM}}$  typically falls within 1–2 times  $r_{\text{sub}}$ , consistent with theoretical expectations and previous observations (e.g. Kishimoto et al. 2007; Koshida et al. 2014). The spectral energy distribution (SED) of the hot dust emission has also been studied by many observational (e.g. Nenkova et al. 2008b; Mor & Netzer 2012; Lani et al. 2017; Shangquan et al. 2018; Zhuang et al. 2018) and theoretical works (e.g. Fritz et al. 2006; Nenkova et al. 2008a; Hönig & Kishimoto 2010, 2017). The SED of the hot dust emission is affected by  $\alpha$  and  $\beta$  because the dust grains further from the heating source have lower tem-

perature. As discussed in Appendix B, the NIR colors of our model are largely consistent with the radiation transfer model (CAT3D; Hönig & Kishimoto 2017) when  $-0.5 < \alpha < 2.0$  and  $0.5 < \beta < 1.5$ . Moreover, we calculate the geometric covering factor of the bowl-shape structure based on the maximum  $h/r$  of the clouds,  $c_f = (h/r)_{\text{max}} / \sqrt{1 + (h/r)_{\text{max}}^2}$ . The  $c_f$  only depends on  $\beta$  because we assume the 2-D surface is fully filled for simplicity in Figure 5. When  $\beta$  increases, the accretion disk is more likely to be obscured by the dust, namely the covering factor  $c_f$  is higher, because more solid angle is covered by the dusty structure. Various observations indicate the dust covering factor is typically 0.6–0.8, for example from the fraction of obscured AGNs (Huchra & Burg 1992; Ricci et al. 2017), dust reprocessed AGN luminosity fraction (Stalevski et al. 2016), and



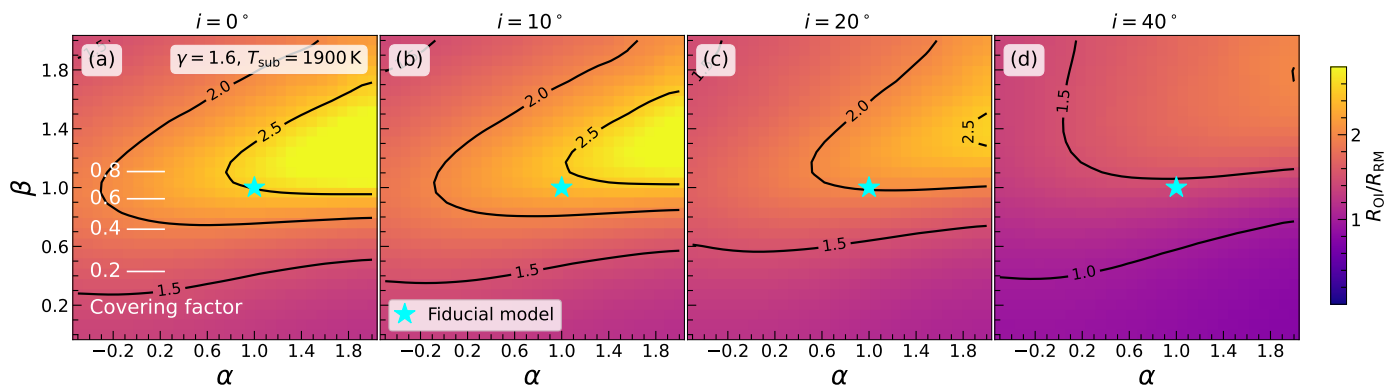


**Fig. 5.** Explore the parameter space of the hot dust structure model. The color maps show the derived  $R_{OI}/R_{RM}$  ratio based on different  $\alpha$  and  $\beta$  in grids. The four columns present the model with different inclination angles ( $i$  from  $0^\circ$  to  $40^\circ$ ). The geometric covering factor of the model is labeled on the left. A fiducial model, which can qualitatively explain our observed  $R_{OI}/R_{RM} \approx 2$ , is indicated by the cyan star.

modeling the X-ray spectrum (Zhao et al. 2021). We find that in the model, the geometric covering factor is  $\sim 0.7$  when  $\beta \approx 1.0$ , consistent with the observations.

The ratio  $R_{OI}/R_{RM}$  in our sample appears relatively constant across the entire luminosity range, yet intriguing variations might arise depending on other properties of the AGN. Ricci et al. (2017) found that the dust covering factor of AGNs with a high Eddington ratio (e.g.  $\lambda_{Edd} \gtrsim 0.1$ ) is much lower than the low Eddington ratio AGNs. In the context of our model, this means  $\beta$  decreases significantly when  $\lambda_{Edd} > 0.1$ . Since the  $R_{OI}/R_{RM}$  is sensitive to  $\beta$ , we expect to find low  $R_{OI}/R_{RM}$  for sources with high  $\lambda_{Edd}$ . However, the current small sample size does not allow for robust statistical analysis on this. More observations of high-Eddington ratio AGNs will be valuable in exploring this dependence. In addition, the model suggests that there is an inclination dependence of  $R_{OI}/R_{RM}$ . It would be also interesting to investigate the relationship between inclination and  $R_{OI}/R_{RM}$  by gathering independent estimations of inclination for a statistically significant sample.

In summary, we conducted a heuristic search of the parameter space of a simple hot dust model to find where  $R_{OI}/R_{RM}$  is around 2. We find a bowl-shape dust emitting structure can explain the observed values with the ratio primarily affected by the inclination angle and  $\beta$  of the model. Moreover, the covering factor of the preferred model is consistent with other independent observations. Our modeling illustrates that combining the OI and RM observations is powerful to constrain the structure of the hot dust emission. The geometric distance based on the joint analysis of the OI and RM observations should account for variation of inclination and opening angle of the bowl-shape for individual sources.

## 6. Summary

1. We present new measurements of the hot dust structure sizes of 14 type 1 AGNs from VLTI/GRAVITY interferometric observation. The typical FWHM is  $\sim 0.7$  mas, comparable to previous near-infrared sizes, and 10-20 times smaller than mid-infrared sizes in the literature.
2. We compiled a sample of 25 AGNs at  $z \lesssim 0.2$  with hot dust sizes measured by optical/infrared interferometry, covering four orders of magnitude in luminosity, to study the  $R-L$  relation. We also compile a sample of 29 AGNs at comparable redshifts with RM measured continuum sizes for comparison. The analysis shows a tight correlation between the size

of the innermost hot dust structure and AGN luminosity, with an intrinsic scatter of less than 0.2 dex, consistent for both OI and RM measured relations.

3. The slopes of the OI and RM  $R-L$  relations are consistent with the canonical value of 0.5 ( $R \propto L^{0.5}$ ) within  $1-\sigma$  if we adopt more accurately derived bolometric luminosity with non-linearity correction. Meanwhile, we find the slope of the relation deviates from 0.5 most significantly with the optical luminosity. We emphasize that proper bolometric corrections should be used when one investigates the  $R-L$  relation.
4. Converted to physical sizes, our direct measurements from GRAVITY show an offset of a factor 2 compared to the equivalent relation derived through reverberation mapping. We use a simple model to explore dust structure geometry, and conclude that a bowl-shape hot dust structure could explain the size ratio in harmony with other physical constraints.

*Acknowledgements.* This research has used the NASA/IPAC Extragalactic Database (NED), operated by the California Institute of Technology, under contract with the National Aeronautics and Space Administration. This research has used the SIMBAD database, operated at CDS, Strasbourg, France.

## References

- Abuter, R., Allouche, F., Amorim, A., et al. 2024, arXiv e-prints, arXiv:2401.14567
- Antonucci, R. R. J. & Miller, J. S. 1985, *ApJ*, 297, 621
- Asmus, D., Gandhi, P., Smette, A., Hönl, S. F., & Duschl, W. J. 2011, *A&A*, 536, A36
- Asmus, D., Hönl, S. F., Gandhi, P., Smette, A., & Duschl, W. J. 2014, *MNRAS*, 439, 1648
- Baldassare, V. F., Reines, A. E., Gallo, E., & Greene, J. E. 2015, *ApJ*, 809, L14
- Barvainis, R. 1987, *ApJ*, 320, 537
- Baumgartner, W. H., Tueller, J., Markwardt, C. B., et al. 2013, *ApJS*, 207, 19
- Burtscher, L., Meisenheimer, K., Tristram, K. R. W., et al. 2013, *A&A*, 558, A149
- Chen, Y.-J., Liu, J.-R., Zhai, S., et al. 2023, *MNRAS*, 522, 3439
- Clavel, J., Wamsteker, W., & Glass, I. S. 1989, *ApJ*, 337, 236
- Duras, F., Bongiorno, A., Ricci, F., et al. 2020, *A&A*, 636, A73
- Eisenhauer, F., Monnier, J. D., & Pfuhl, O. 2023, *ARA&A*, 61, 237
- Fernández-Ontiveros, J. A., López-López, X., & Prieto, A. 2023, *A&A*, 670, A22
- Fritz, J., Franceschini, A., & Hatziminaoglou, E. 2006, *MNRAS*, 366, 767
- Gómez Rosas, V., Isbell, J. W., Jaffe, W., et al. 2022, *Nature*, 602, 403
- Goad, M. R., Korista, K. T., & Ruff, A. J. 2012, *MNRAS*, 426, 3086
- GRAVITY Collaboration, Abuter, R., Accardo, M., et al. 2017, *A&A*, 602, A94
- GRAVITY+ Collaboration, Abuter, R., Allouche, F., et al. 2022, *A&A*, 665, A75
- GRAVITY Collaboration, Amorim, A., Bauböck, M., et al. 2021a, *A&A*, 654, A85

- GRAVITY Collaboration, Amorim, A., Bauböck, M., et al. 2021b, *A&A*, 648, A117
- GRAVITY Collaboration, Amorim, A., Bourdarot, G., et al. 2024, arXiv e-prints, arXiv:2401.07676
- GRAVITY Collaboration, Amorim, A., Bourdarot, G., et al. 2023, *A&A*, 669, A14
- GRAVITY Collaboration, Dexter, J., Shangguan, J., et al. 2020a, *A&A*, 635, A92
- GRAVITY Collaboration, Pfuhl, O., Davies, R., et al. 2020b, *A&A*, 634, A1
- GRAVITY Collaboration, Sturm, E., Dexter, J., et al. 2018, *Nature*, 563, 657
- Guise, E., Hönl, S. F., Gorjian, V., et al. 2022, *MNRAS*, 516, 4898
- Hönl, S. F. 2019, *ApJ*, 884, 171
- Hönl, S. F. & Kishimoto, M. 2010, *A&A*, 523, A27
- Hönl, S. F. & Kishimoto, M. 2011, *A&A*, 534, A121
- Hönl, S. F. & Kishimoto, M. 2017, *ApJ*, 838, L20
- Hönl, S. F., Kishimoto, M., Tristram, K. R. W., et al. 2013, *ApJ*, 771, 87
- Huchra, J. & Burg, R. 1992, *ApJ*, 393, 90
- Kawaguchi, T. & Mori, M. 2010, *ApJ*, 724, L183
- Kelly, B. C. 2007, *ApJ*, 665, 1489
- Kishimoto, M., Anderson, M., ten Brummelaar, T., et al. 2022, *ApJ*, 940, 28
- Kishimoto, M., Hönl, S. F., Antonucci, R., et al. 2011a, *A&A*, 527, A121
- Kishimoto, M., Hönl, S. F., Antonucci, R., et al. 2009, *A&A*, 507, L57
- Kishimoto, M., Hönl, S. F., Antonucci, R., et al. 2013, *ApJ*, 775, L36
- Kishimoto, M., Hönl, S. F., Antonucci, R., et al. 2011b, *A&A*, 536, A78
- Kishimoto, M., Hönl, S. F., Beckert, T., & Weigelt, G. 2007, *A&A*, 476, 713
- Koshida, S., Minezaki, T., Yoshii, Y., et al. 2014, *ApJ*, 788, 159
- Koss, M., Trakhtenbrot, B., Ricci, C., et al. 2017, *ApJ*, 850, 74
- Lani, C., Netzer, H., & Lutz, D. 2017, *MNRAS*, 471, 59
- Lapeyriere, V., Kervella, P., Lacour, S., et al. 2014, in *Society of Photo-Optical Instrumentation Engineers (SPIE) Conference Series*, Vol. 9146, *Optical and Infrared Interferometry IV*, ed. J. K. Rajagopal, M. J. Creech-Eakman, & F. Malbet, 91462D
- Leftley, J., Petrov, R., Moszczynski, N., et al. 2023, arXiv e-prints, arXiv:2312.12125
- Leftley, J. H., Tristram, K. R. W., Hönl, S. F., et al. 2021, *ApJ*, 912, 96
- Leftley, J. H., Tristram, K. R. W., Hönl, S. F., et al. 2018, *ApJ*, 862, 17
- López-Gonzaga, N., Burtscher, L., Tristram, K. R. W., Meisenheimer, K., & Schartmann, M. 2016, *A&A*, 591, A47
- Lyu, J., Rieke, G. H., & Smith, P. S. 2019, *ApJ*, 886, 33
- Mandal, A. K., Woo, J.-H., Wang, S., et al. 2024, arXiv e-prints, arXiv:2403.01885
- Marconi, A., Risaliti, G., Gilli, R., et al. 2004, *MNRAS*, 351, 169
- McConnell, N. J., Ma, C.-P., Gebhardt, K., et al. 2011, *Nature*, 480, 215
- Mehrgan, K., Thomas, J., Saglia, R., et al. 2019, *ApJ*, 887, 195
- Mezcua, M. & Sánchez, H. D. 2024, *MNRAS*[arXiv:2401.15152]
- Minezaki, T., Yoshii, Y., Kobayashi, Y., et al. 2019, *ApJ*, 886, 150
- Mor, R. & Netzer, H. 2012, *MNRAS*, 420, 526
- Neškova, M., Sirocky, M. M., Ivezić, Ž., & Elitzur, M. 2008a, *ApJ*, 685, 147
- Neškova, M., Sirocky, M. M., Nikutta, R., Ivezić, Ž., & Elitzur, M. 2008b, *ApJ*, 685, 160
- Netzer, H. 2015, *ARA&A*, 53, 365
- Netzer, H. 2019, *MNRAS*, 488, 5185
- Oknyansky, V. L., Gaskell, C. M., & Shimanovskaya, E. V. 2015, *Odessa Astronomical Publications*, 28, 175
- Planck Collaboration, Ade, P. A. R., Aghanim, N., et al. 2016, *A&A*, 594, A13
- Pott, J.-U., Malkan, M. A., Elitzur, M., et al. 2010, *ApJ*, 715, 736
- Pozo Nuñez, F., Haas, M., Chini, R., et al. 2014, *A&A*, 561, L8
- Prieto, M. A., Nadolny, J., Fernández-Ontiveros, J. A., & Mezcua, M. 2021, *MNRAS*, 506, 562
- Prieto, M. A., Reunanen, J., Tristram, K. R. W., et al. 2010, *MNRAS*, 402, 724
- Ramolla, M., Haas, M., Westhues, C., et al. 2018, *A&A*, 620, A137
- Reines, A. E. 2022, *Nature Astronomy*, 6, 26
- Ricci, C., Trakhtenbrot, B., Koss, M. J., et al. 2017, *Nature*, 549, 488
- Shakura, N. I. & Sunyaev, R. A. 1973, *A&A*, 24, 337
- Shangguan, J., Ho, L. C., & Xie, Y. 2018, *ApJ*, 854, 158
- Sobrino Figaredo, C., Haas, M., Ramolla, M., et al. 2020, *AJ*, 159, 259
- Stalevski, M., Ricci, C., Ueda, Y., et al. 2016, *MNRAS*, 458, 2288
- Suganuma, M., Yoshii, Y., Kobayashi, Y., et al. 2006, *ApJ*, 639, 46
- Swain, M., Vasisht, G., Akesson, R., et al. 2003, *ApJ*, 596, L163
- Trakhtenbrot, B., Ricci, C., Koss, M. J., et al. 2017, *MNRAS*, 470, 800
- Urry, C. M. & Padovani, P. 1995, *PASP*, 107, 803
- Vasudevan, R. V. & Fabian, A. C. 2007, *MNRAS*, 381, 1235
- Vasudevan, R. V. & Fabian, A. C. 2009, *MNRAS*, 392, 1124
- Vignali, C., Brandt, W. N., & Schneider, D. P. 2003, *AJ*, 125, 433
- Weigelt, G., Hofmann, K. H., Kishimoto, M., et al. 2012, *A&A*, 541, L9
- Winter, L. M., Mushotzky, R. F., Reynolds, C. S., & Tueller, J. 2009, *ApJ*, 690, 1322
- Winter, L. M., Veilleux, S., McKernan, B., & Kallman, T. R. 2012, *ApJ*, 745, 107
- Wright, E. L., Eisenhardt, P. R. M., Mainzer, A. K., et al. 2010, *AJ*, 140, 1868
- Yang, Q., Shen, Y., Liu, X., et al. 2020, *ApJ*, 900, 58
- Zhao, X., Marchesi, S., Ajello, M., et al. 2021, *A&A*, 650, A57
- Zhuang, M.-Y., Ho, L. C., & Shangguan, J. 2018, *ApJ*, 862, 118

- 
- <sup>1</sup> Universidade de Lisboa - Faculdade de Ciências, Campo Grande, 1749-016 Lisboa, Portugal
  - <sup>2</sup> CENTRA - Centro de Astrofísica e Gravitação, IST, Universidade de Lisboa, 1049-001 Lisboa, Portugal
  - <sup>3</sup> Max Planck Institute for Extraterrestrial Physics (MPE), Giessenbachstr.1, 85748 Garching, Germany
  - <sup>4</sup> Max Planck Institute for Astronomy, Königstuhl 17, 69117, Heidelberg, Germany
  - <sup>5</sup> LESIA, Observatoire de Paris, Université PSL, CNRS, Sorbonne Université, Univ. Paris Diderot, Sorbonne Paris Cité, 5 place Jules Janssen, 92195 Meudon, France
  - <sup>6</sup> Leiden University, 2311EZ Leiden, The Netherlands
  - <sup>7</sup> Department of Astrophysical & Planetary Sciences, JILA, University of Colorado, Duane Physics Bldg., 2000 Colorado Ave, Boulder, CO 80309, USA
  - <sup>8</sup> I. Institute of Physics, University of Cologne, Zùlpicher Straße 77, 50937 Cologne, Germany
  - <sup>9</sup> Max Planck Institute for Radio Astronomy, Auf dem Hügel 69, 53121 Bonn, Germany
  - <sup>10</sup> European Southern Observatory, Alonso de Córdova 3107, Casilla 19001, Vitacura, Santiago, Chile
  - <sup>11</sup> Faculdade de Engenharia, Universidade do Porto, rua Dr. Roberto Frias, 4200-465 Porto, Portugal
  - <sup>12</sup> Departments of Physics and Astronomy, Le Conte Hall, University of California, Berkeley, CA 94720, USA
  - <sup>13</sup> Research School of Astronomy and Astrophysics, Australian National University, Canberra, ACT 2611, Australia
  - <sup>14</sup> Department of Physics and Astronomy, University of Southampton, Southampton, UK
  - <sup>15</sup> Department of Physics, Kyoto Sangyo University, Kita-ku, Japan
  - <sup>16</sup> European Southern Observatory, Karl-Schwarzschild-Str. 2, 85748 Garching, Germany
  - <sup>17</sup> Université Côte d'Azur, Observatoire de la Côte d'Azur, CNRS, Laboratoire Lagrange, Nice, France
  - <sup>18</sup> School of Physics and Astronomy, Tel Aviv University, Tel Aviv 69978, Israel
  - <sup>19</sup> Univ. Grenoble Alpes, CNRS, IPAG, 38000 Grenoble, France
  - <sup>20</sup> Retired
  - <sup>21</sup> Instituto de Astrofísica de Canarias (IAC), E-38205 La Laguna, Tenerife, Spain
  - <sup>22</sup> Center for Computational Astrophysics, Flatiron Institute, 162 5th Ave., New York, NY 10010, USA

## Appendix A: Bolometric luminosity correction

We convert each type of measured luminosity to the bolometric luminosity, using non-linear corrections, following the same method as GRAVITY Collaboration et al. (2020a). We collect the 14–195 keV flux from the 70-month *Swift*-BAT survey catalogue (Baumgartner et al. 2013). We mainly use  $L_{14-195 \text{ keV}}$  to calculate the bolometric luminosity following the relation from Winter et al. (2012), which is derived using bolometric luminosities from optical-to-X-ray SED fitting (Vasudevan & Fabian 2007, 2009),

$$\log\left(\frac{L_{\text{bol},14-195 \text{ keV}}}{\text{erg s}^{-1}}\right) = 1.1157 \log\left(\frac{L_{14-195 \text{ keV}}}{\text{erg s}^{-1}}\right) - 4.2280. \quad (\text{A.1})$$

We also use monochromatic luminosity at  $5100\text{\AA}$  following the relation in Trakhtenbrot et al. (2017),

$$\log\left(\frac{L_{\text{bol},5100 \text{\AA}}}{\text{erg s}^{-1}}\right) = 0.916 \log\left(\frac{\lambda L_{\lambda}(5100 \text{\AA})}{\text{erg s}^{-1}}\right) + 4.596. \quad (\text{A.2})$$

This relation was obtained using the bolometric correction for the *B* band from Marconi et al. (2004) based on luminosity-dependent SED templates, and additionally assuming a constant UV-to-optical spectral slope for the conversion from *B* band correction to  $5100\text{\AA}$ .

For the MIR flux, we first convert  $12 \mu\text{m}$  flux  $f_{12 \mu\text{m}}$  to 2 – 10 keV flux  $f_{2-10 \text{ keV}}$  following Asmus et al. (2011),

$$\log\left(\frac{f_{2-10 \text{ keV}}}{\text{erg s}^{-1} \text{ cm}^{-2}}\right) = 0.89 \log\left(\frac{f_{12 \mu\text{m}}}{\text{mJy}}\right) - 12.81, \quad (\text{A.3})$$

then  $L_{14-195 \text{ keV}}$  is calculated from 2 – 10 keV luminosity using the relation from Winter et al. (2009),

$$\log\left(\frac{L_{14-195 \text{ keV}}}{\text{erg s}^{-1}}\right) = 0.94 \log\left(\frac{L_{2-10 \text{ keV}}}{\text{erg s}^{-1}}\right) + 2.91. \quad (\text{A.4})$$

Both of the relations are established empirically. Finally the MIR-based bolometric luminosity  $L_{\text{bol},12 \mu\text{m}}$  is obtained using Equation A.1.

We list the results of the bolometric luminosities calculated from the above methods in Table A.1. We compare the three different bolometric luminosities in Figure A.1. We find that the differences are within 0.3 dex, and we use this value as the uncertainty of bolometric luminosities. The variability effect is partially captured within this uncertainty since the luminosities at different bands are collected at different times.

The bolometric luminosities adopted for studying the  $R-L_{\text{bol}}$  relation in this work are listed in column (10) of Table A.1. We prioritize  $L_{14-195 \text{ keV}}$ -based bolometric luminosity; when it is unavailable,  $\lambda L_{\lambda}(5100\text{\AA})$ -based calculation is used. This preference is due to the  $L_{14-195 \text{ keV}}$ -based correction being established with bolometric luminosities reliably determined from SED fitting, whereas additional SED model assumptions were required for the  $\lambda L_{\lambda}(5100\text{\AA})$ -based calculations, potentially leading to extra uncertainties. The  $\lambda L_{\lambda}(12\mu\text{m})$ -based bolometric calculation incorporated two empirical relations in addition to the one between  $L_{\text{bol}}$  and 14–195 keV luminosity, making it potentially less reliable; therefore, we use it only for comparative evaluations. For AGNs common with those studied by Prieto et al. (2010), the bolometric luminosities we adopted are consistent with those derived from nuclear SEDs by those authors.

## Appendix B: The torus model

Following Guise et al. (2022), we build a torus model to simulate the hot dust emission and time lag in *K* band. Our primary goal is to investigate whether the observed  $R_{\text{OI}}/R_{\text{RM}} \approx 2$  can be explained by a simple model. The model has been discussed comprehensively in Guise et al. (2022). We briefly summarize its key points and clarify our treatments that are different from Guise et al. (2022).

The torus model consists of a large number of dust clouds randomly generated to form a 2D surface. The radial distribution of the clouds follows a power-law probability density function (PDF),

$$\text{PDF}(r) \propto \left(\frac{r}{r_{\text{sub}}}\right)^{\alpha}, \quad (\text{B.1})$$

where  $r$  is radial distance of cloud from the center,  $r_{\text{sub}}$  is the sublimation radius of the dust, and power-law index,  $\alpha$ , is a primary free parameter of the model. The underlying radial density of clouds thus follows a power-law with an index of  $\alpha-1$ ; a value of  $\alpha = 1$  means a flat density profile at any radius, while a higher  $\alpha$  means more clouds distribute to larger distances. We adopted the maximum radius of the clouds to be 20 times that of  $r_{\text{sub}}$ . However,  $R_{\text{OI}}/R_{\text{RM}}$  is not sensitive to the maximum radius because both  $R_{\text{OI}}$  and  $R_{\text{RM}}$  increase with the maximum radius. The height of the clouds above the midplane,  $h$ , follows a power-law function,

$$h = r_{\text{sub}} \left[ \left(\frac{r}{r_{\text{sub}}}\right)^{\beta} - 1 \right], \quad (\text{B.2})$$

where the power-law index  $\beta$  is another primary parameter of this model. The model is close to a flat disk when  $\beta$  is close to 0, and is close to parabolic when  $\beta = 2$ . Although the dust torus may have a more complicated 3D structure (Hönig 2019), the *K*-band emission is expected to be emitted from the hottest dust close to the surface of the torus facing the radiation from the accretion disk. Considering the effect of illumination, we include the emission weight of the clouds,

$$\kappa = 0.5(1 - \cos \psi), \quad (\text{B.3})$$

where  $\psi$  is the angle between observer's line of sight and cloud's line of sight to the center from the origin (the radiation source). Each dust cloud is assumed to have black body emission in a equilibrium state according to the absorbed emission from the central radiation source, so the dust temperature is,

$$T(r) = T_{\text{sub}} \left(\frac{r}{r_{\text{sub}}}\right)^{\frac{-2}{4+\gamma}}, \quad (\text{B.4})$$

where  $r$  is the radius of the dust cloud,  $T_{\text{sub}}$  is the sublimation temperature, and  $\gamma$  is the dust IR opacity power-law index which is around 1–2 for interstellar dust. We adopt  $\gamma = 1.6$  for typical astronomical dust following Barvainis (1987), while we find that our conclusions are not sensitive to the adopted  $\gamma$ . We choose to use  $T_{\text{sub}} = 1900 \text{ K}$ , instead of  $1500 \text{ K}$  adopted by Barvainis (1987), because recent observations found increasing evidence of a higher sublimation temperature due to the graphite dust grains (Mor & Netzer 2012; Hönig & Kishimoto 2017). Our model  $R_{\text{OI}}/R_{\text{RM}}$  is not very sensitive to the  $T_{\text{sub}}$ , but as discussed later, we find our model provides consistent *JHK* color when adopting  $T_{\text{sub}} = 1900 \text{ K}$ .

In order to calculate the  $R_{\text{OI}}$ , we first simulate the observed visibility of the dust torus model with the realistic baseline

**Table A.1.** Properties of the AGNs used in this work.

Source	$z$	$L_{14-195\text{keV}}$ (erg s <sup>-1</sup> )	$\lambda L_{\lambda}(5100\text{\AA})$ (erg s <sup>-1</sup> )	$\lambda L_{\lambda}(12\mu\text{m})$ (erg s <sup>-1</sup> )	$\log L_{\text{bol},14-195\text{keV}}$ (erg s <sup>-1</sup> )	$\log L_{\text{bol},5100\text{\AA}}$ (erg s <sup>-1</sup> )	$\log L_{\text{bol},12\mu\text{m}}$ (erg s <sup>-1</sup> )	$\log L_{\text{bol}}$ (erg s <sup>-1</sup> )	$\log M_{\text{BH}}$ (M <sub>⊙</sub> )	$\log \lambda_{\text{Edd}}$
(1)	(2)	(3)	(4)	(5)	(6)	(7)	(8)	(9)	(10)	(11)
3C 120	0.033	44.4	44.0	44.2	45.3	44.9	44.9	45.3	7.5	-0.29
3C 273	0.158	...	45.9	45.7	...	46.6	46.5	46.6	8.5	0.03
Akn 120	0.033	44.3	43.9	44.2	45.2	44.8	44.9	45.2	8.4	-1.40
ESO 323-G77	0.015	43.2	43.1	43.7	44.0	44.1	44.3	44.0	7.1	-1.20
GQ Com	0.165	44.9	44.6	...	45.9	45.5	...	45.9	8.3	-0.54
H0507+164	0.018	43.8	42.6	...	44.7	43.6	...	44.7	7.0	-0.41
HE 1029-1401	0.086	44.8	44.6	...	45.8	45.5	...	45.8	8.7	-1.08
IC 4329A	0.016	44.3	43.5	44.2	45.1	44.4	44.9	45.1	8.2	-1.13
IRAS 03450+0055	0.032	...	43.9	...	...	44.8	...	44.8	7.8	-1.07
IRAS 09149-6206	0.057	44.4	45.0	45.0	45.3	45.8	45.7	45.3	8.1	-0.83
IRAS 13349+2438	0.108	...	45.0	45.6	...	45.8	46.3	45.8	7.8	-0.12
MCG+08-11-011	0.021	44.1	43.3	...	45.0	44.3	...	45.0	7.7	-0.82
MCG-6-30-15	0.008	43.0	41.6	43.1	43.7	42.7	43.7	43.7	6.6	-1.04
Mrk 110	0.035	44.2	43.7	...	45.1	44.6	...	45.1	7.1	-0.10
Mrk 1239	0.020	...	44.5	44.1	...	45.4	44.8	45.4	6.4	0.85
Mrk 231	0.042	...	45.0	45.2	...	45.8	45.9	45.8	7.9	-0.16
Mrk 335	0.026	43.5	43.8	...	44.3	44.7	...	44.3	6.9	-0.73
Mrk 509	0.034	44.5	44.2	44.3	45.4	45.1	45.0	45.4	8.2	-0.90
Mrk 590	0.026	43.5	43.5	43.6	44.2	44.4	44.3	44.2	7.6	-1.43
Mrk 6	0.019	43.7	43.6	...	44.6	44.5	...	44.6	8.0	-1.56
Mrk 744	0.009	42.5	41.8	...	43.2	42.9	...	43.2	7.4	-2.26
Mrk 79	0.022	43.7	43.7	...	44.6	44.6	...	44.6	7.8	-1.37
Mrk 817	0.031	43.8	43.7	...	44.6	44.6	...	44.6	8.1	-1.53
NGC 1365	0.005	42.7	41.9	42.8	43.4	43.0	43.4	43.4	6.3	-1.00
NGC 3227	0.004	42.6	42.2	42.2	43.3	43.2	42.8	43.3	7.1	-1.94
NGC 3516	0.009	43.3	42.8	...	44.1	43.8	...	44.1	7.8	-1.81
NGC 3783	0.010	43.6	43.0	43.6	44.4	44.0	44.2	44.4	7.6	-1.27
NGC 4051	0.002	41.7	41.9	42.2	42.3	43.0	42.7	42.3	5.7	-1.50
NGC 4151	0.003	43.1	42.1	42.9	43.9	43.2	43.5	43.9	7.7	-1.93
NGC 4593	0.008	43.2	42.6	43.0	43.9	43.6	43.6	43.9	7.3	-1.50
NGC 5548	0.017	43.8	43.3	43.3	44.6	44.3	44.0	44.6	8.2	-1.68
NGC 7469	0.016	43.6	43.5	43.9	44.5	44.4	44.5	44.5	7.6	-1.26
NGC 7603	0.029	44.0	44.4	...	44.9	45.3	...	44.9	8.4	-1.65
PDS 456	0.184	...	46.3	45.9	...	47.0	46.6	47.0	8.7	0.22
PG 0844+349	0.064	...	44.2	44.0	...	45.1	44.8	45.1	7.7	-0.69
PG 0953+414	0.234	...	45.2	...	...	46.0	...	46.0	8.4	-0.55
PG 1613+658	0.121	44.7	44.8	...	45.6	45.6	...	45.6	8.8	-1.27
PGC 50427	0.024	43.4	43.1	...	44.1	44.1	...	44.1	7.3	-1.30
PGC 89171	0.027	43.5	43.9	...	44.4	44.8	...	44.4	7.6	-1.36
UGC 11763	0.063	...	44.3	44.7	...	45.2	45.4	45.2	7.3	-0.23
UGC 545	0.061	...	44.5	45.0	...	45.4	45.7	45.4	7.0	0.28
WPVS 48	0.037	...	43.6	...	...	44.5	...	44.5	7.0	-0.57
Z 229-15	0.028	...	42.9	...	...	43.9	...	43.9	6.9	-1.15

**Notes.** (1) Source name. (2) Redshift from NED. (3) X-ray 14-195 keV 70-month *Swift*-BAT survey catalogue (Baumgartner et al. 2013) (4) optical luminosity at 5100 Å  $\lambda L_{\lambda}(5100\text{\AA})$  collected from the BASS catalogue (Koss et al. 2017). (5) 12 μm luminosity  $\lambda L_{\lambda}(12\mu\text{m})$  from Asmus et al. (2014). (6) Bolometric luminosity derived from  $L_{14-195\text{keV}}$  using Equation A.1. (7) Bolometric luminosity derived from  $\lambda L_{\lambda}(5100\text{\AA})$  using Equation A.2. (8) Bolometric luminosity derived from  $\lambda L_{\lambda}(12\mu\text{m})$  using Equations A.3, A.4 and A.1. (9) The adopted bolometric luminosity in this work:  $L_{\text{bol},14-195\text{keV}}$  is preferred; when it is unavailable,  $L_{\text{bol},5100\text{\AA}}$  is adopted. (10) Black hole mass from GRAVITY Collaboration et al. (2023). (11) Eddington ratio calculated from columns (9) and (10).

lengths of GRAVITY and apply the same fitting method as described in Section 3. The torus time lag is calculated as the flux-weighted mean time lag of each cloud.<sup>3</sup> In this work, we use the model in a heuristic manner to investigate whether there is a parameter range that can explain our observed  $R_{\text{OI}}/R_{\text{RM}}$ . We explored mainly the parameter space defined in Guise et al. (2022). We found that  $\alpha \approx 1.0$  is preferred to obtain  $R_{\text{OI}}/R_{\text{RM}} \approx 2$ , much larger than the parameter range defined in Guise et al. (2022) ( $-5.5 < \alpha < -0.5$ ). The  $\alpha$  controls the radial distribution of the dust clouds so it influences the SED of the model. Our pre-

ferred  $\alpha$  ranges are not necessary the same as theirs since we are focusing on *K* band observations, while Guise et al. (2022) are working in longer wavelengths. We compare the *JHK* colors predicted by our model to the CAT3D model (Hönig & Kishimoto 2017), one of the state-of-the-art torus models considering different temperatures of the graphite and silicon dust and the polar wind structure. We focus on the *JHK* colors because, unlike CAT3D, our model only consider the hottest dust in the torus surface. As shown in Figure B.1, the *J - H* and *H - K*

<sup>3</sup> The time lag of the *i*th cloud is  $\tau_i = r_i(1 - \cos \psi_i)$ .



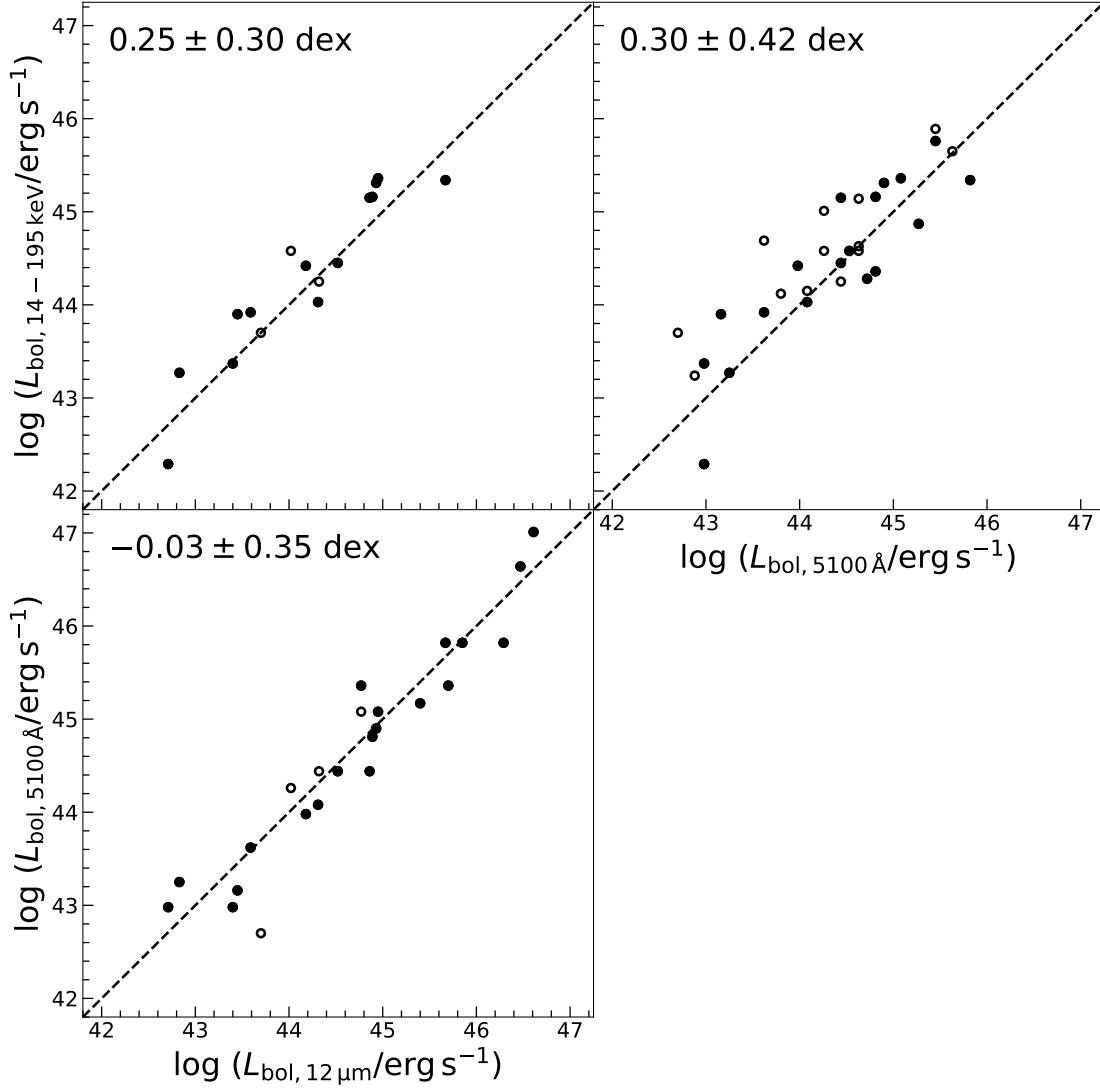


**Fig. A.1.** Comparisons of  $L_{\text{bol}}$  corrections from different measurements. The solid dots highlight the sources with OI measured sizes. The dashed lines show the one-to-one relation. The median and standard deviation of  $y - x$  are shown in the top-left corner in each panel.

colors of our simple model matches those of the CAT3D model<sup>4</sup> in the parameter ranges that we adopt in this work, in particular,  $-0.5 < \alpha < 2$ . We also find that our model will become much redder than the CAT3D model if we use  $T_{\text{sub}} = 1500$  K, likely because that the CAT3D model includes the graphite dust with the sublimation temperature at 1900 K. The comparison with *JHK* colors suggest that the dust distribution of our model is reasonable. The conclusion is not sensitive to the choice of the radiative transfer model as long as the  $T_{\text{sub}}$  is assumed consistently. We prefer to compare our model colors with the radiative transfer models over the real observation because the observed AGN SED are contaminated by the host galaxy which is usually bright in NIR. In summary, we confirm that our adopted parameter ranges align with the theoretically expected color of the torus.

<sup>4</sup> Some CAT3D models show a low  $J - H$  color (e.g. at  $1.2 < H - K < 1.8$ ) primarily because the accretion disk emission contaminates the color when the torus emission is very red.

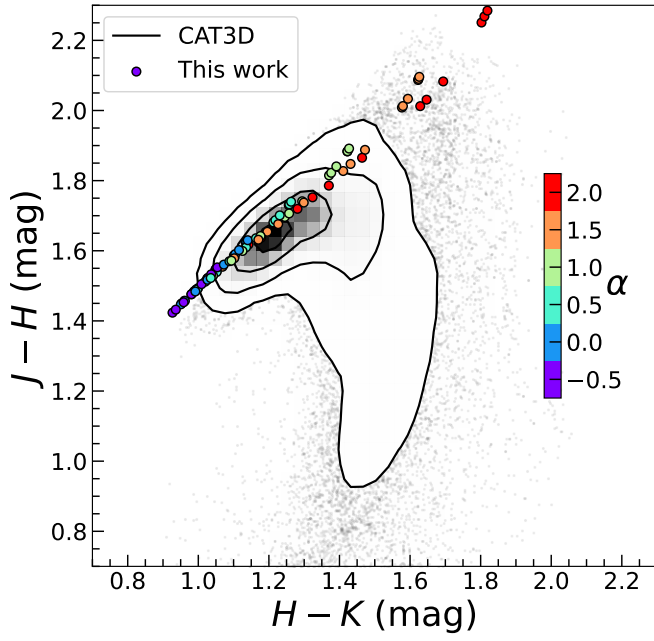


**Fig. B.1.** The  $J-H$  and  $H-K$ , relation of our torus model (color-coded) comparing that of the CAT3D-wind model (in black). We calculated our torus model with  $-0.5 < \alpha < 2.0$ ,  $0.5 < \beta < 1.5$ , and  $i < 40^\circ$ . We include the CAT3D-wind model SEDs with  $i < 45^\circ$  for comparison.